Junction Temperature Optimization Based Compensation Strategy of Modular Multilevel Railway Power Conditioner

Hongqi Ding, *Student Member, IEEE*, Fujun Ma, *Senior Member, IEEE*, Rong Han, *Student Member, IEEE*, Lei Wang, *Senior Member, IEEE*, Liheng Lin, and Qianming Xu, *Member, IEEE*

***Abstract*—The modular multilevel railway power conditioner (MM-RPC) can effectively improve the power quality of the railway power grid. However, since the operating conditions of MM-RPC frequently vary with the traction load, the junction temperatures of semiconductor devices fluctuate very drastically. Severe junction temperature swings can easily affect the service lifetime and reliability of the MM-RPC. In this article, a power hysteresis based on incomplete compensation control strategy is proposed. The proposed control can effectively reduce junction temperature fluctuations under complex mission profiles and increase the overall life of the system while meeting the power quality requirements. Furthermore, the effectiveness of the proposed control is verified in MATLAB/PLECS electrothermal cosimulation under a section of the load curve of the Beijing–Shanghai high-speed railway traction substation. Finally, the experimental thermal platform is built to validate the effectiveness of the proposed control strategy.**

***Index Terms*—Active thermal control (ATC), incomplete compensation, railway power conditioner.**

I. Introduction

HIGH-SPEED trains have the advantages of fast, stability, and comfort, which greatly facilitate people's travel. However, many power quality problems occur in single-phase traction power supply (STPS) for high-speed railways, such as negative sequence current and low power factor [1]–[3]. Therefore, the power quality compensation equipment of the railway power supply system has received increasing attention.

Various solutions are proposed to improve the power quality of the STPS system by scholars. In [4], a balanced transformer is introduced in the STPS, but its suppression ability is limited. In addition, the increased capacity of the traction system is regarded as an effective measure in [5] and [6]. Even if the imbalance tolerance of the system is increased and the grid-side power quality standard is reached, the power factor of the system is still low. Passive in [7] and active compensation equipment [8] are added to tackle the low power factor. But only specific harmonics and reactive power can be eliminated in [7] and a large-capacity step-down transformer is needed in [8]. Therefore, there is an urgent need for equipment that can not only improve the power factor but also compensate for the negative sequence imbalance. A modular multilevel railway power conditioner (MM-RPC) is a satisfying equipment that has a comprehensive compensation performance, flexible system without step-down power-frequency transformer, and modular structure [9]. Therefore, this article focuses on the research around MM-RPC.

As the ac grid voltage level increases, the number of submodules (SMs) of MM-RPC increases significantly. In addition to improving output performance, the reliability of equipment is gradually drawing the attentions of experts and scholars. According to the statistics in [10], it can be shown that the reliability of the converter is affected by factors, such as temperature, humidity, and vibration. However, device failures caused by temperature are as high as 55% of converter failures, which accounts for the highest proportion. Especially in high-voltage and high-power systems, it is particularly significant to ensure the long-term safe and reliable operation of the equipment. For MM-RPC, the power transmitted between the two traction feeders frequently varied with the operating conditions of the locomotive load. Thus, the converters on both traction feeders of MM-RPC operate between the rectification state and the inversion state at any time. This causes junction temperature fluctuations in SMs devices, which seriously decreases the number of cycles before failure of the device. The reduction in the number of cycles means that the lifetime of the device is reduced [11].

Therefore, many scholars are currently devoted to the research of active thermal control (ATC). Among them, some studies improve the junction temperature by changing the modulation strategy. A flat-top method is applied in [12], which can be used to shift the neutral point potential to reduce thermal cycles. The active clamping angle based on discontinuous pulsewidth modulation (DPWM) is employed in [13]. The clamping angle is controlled for regulating switching loss, which prolongs the remaining useful lifetime of the power semiconductor. The hybrid discontinuous modulation technology is proposed in

Manuscript received July 12, 2021; revised November 5, 2021; accepted December 24, 2021. Date of publication January 7, 2022; date of current version February 18, 2022. This work was supported in part by the National Natural Science Foundation of China under Grant 51977067 and in part by the Natural Science Foundation of Hunan Province under Grants 2019RS2017 and 2020JJ3010. Recommended for publication by Associate Editor B. McGrath. *(Corresponding authors: Fujun Ma; Rong Han.)*

The authors are with the College of Electrical and Information Engineering, Hunan University, Changsha 410082, China (e-mail: s150900718@hnu.edu.cn; mafujun2004@163.com; hanrong@hnu.edu.cn; jordanwanglei@gmail.com; 493121835@qq.com; xqm@hnu.edu.cn).

Color versions of one or more figures in this article are available at https://doi.org/10.1109/TPEL.2021.3139702.

Digital Object Identifier 10.1109/TPEL.2021.3139702

[14]. The space-vector-pulsewidth modulation (SVPWM) and the DPWM are combined with adjusting the switching loss. The finite control set model predictive control is applied in [15], which selects the best switching vector based on multiparameter optimization, reduces the stress caused by thermal cycles. Since the nearest level modulation (NLM) is usually used in high-power multilevel STPS to greatly reduce the switching loss, it is difficult to directly use the existing thermal control of the modulation layer. In addition to the ATC at the modulation level, based on the degree of freedom of thermal control, the loss distribution can also be changed by controlling some control variables, such as circulating current, switching frequency, and capacitor voltage. In [16], a larger circulating current is injected at light load, and less circulating current is injected at heavy load, or even no circulating current is injected. In this way, thermal fluctuations caused by load changes can be reduced. Although circulating current injection can effectively reduce the junction temperature swing of the device, it brings additional losses and leads to an increase in the average junction temperature. In addition, the junction temperature swing can be reduced by selecting the appropriate switching frequency under different mission profiles in [17]. The control strategy of the variable carrier frequency is proposed in [18], which realizes the goal of junction temperature control by adjusting the switching loss. However, the conduction loss dominates the distribution of MM-RPC loss. Therefore, the ability to optimize the junction temperature by changing the switching loss is limited. In addition, there are scholars to improve the thermal performance from the coordinated control of the variables between the converters. In [19], a certain amount of reactive power is introduced between the converters to compensate for the losses of the semiconductor device. The coordinated control strategy is proposed in [20] and [21] for the wind power system and the energy storage system to increase the operating lifetime of the wind power converter. The above-mentioned system-level thermal control is restricted by topology types and profile missions, which results in application limitations.

The above-mentioned junction temperature optimization methods mainly focus on ATC at the control layer or in specific application scenarios, while seldom studies on the junction temperature control of RPC converters based on the operating characteristics of the STPS system. Moreover, due to the changeable and complex profile missions of MM-RPC, the load situation and the operating states can be changed at any time. Thus, the above-mentioned ATC technology is difficult to apply directly.

In order to solve this problem, in view of the characteristics of the operation of the MM-RPC system, a power hysteresis based on incomplete compensation (PHIC) control is proposed in this article. The proposed control can effectively reduce junction temperature fluctuations under complex mission profiles and increase the overall life of the system while meeting the power quality requirements. Therefore, the contributions of this article can be summarized as follows.

1) According to the compensation principle of MM-RPC, the loss model of the MM-RPC power module is established. Based on the loss model, the loss distribution, difference and thermal performance of the four power devices in the module under different operation states are analyzed.
2) A PHIC is proposed, and the junction temperature fluctuation is effectively reduced under the complex mission profile. Finally, the overall lifetime of the system is improved.
3) Under the proposed control, the power quality on the three-phase grid side meets the requirements of the China national standard GB/T 15543-2008. And the electrical characteristics (SM voltage, grid-side voltage, circulating current) of MM-RPC are not affected.

The rest of this article is organized as follows. Section II introduces the main circuit and the working principle of MM-PRC. The distribution characteristics of the SMs devices loss and junction temperature are analyzed in Section III. The proposed PHIC control is described in detail in Section IV. Then, the simulation and experimental results are provided in Sections V and VI, respectively. Finally, Section VII concludes this article.

II. MM-RPC Topology and Working Principle

A. Traction Power Supply System

Compared with the traditional back-to-back RPC, MM-RPC adopts a modular cascade structure and does not require a step-down transformer. Therefore, it shows obvious advantages in terms of volume, weight and flexibility. In addition, the control strategies of the converters on both sides are similar, and the consistency of the SMs currents can be maintained. Therefore, MM-RPC is adopted as the research object in this article. The schematic of the V/v traction power supply system is shown in Fig. 1, with a red dotted frame. *A, B*, and *C* are the three phases of the public grid, and the step-down V/v transformer is used to convert 220 kV into two 27.5 kV traction feeders as the power supply of the α and β arm. Among them, i_{SX} ($X = A, B, C$) is the grid-side three-phase current, i_{Lx} ($x = \alpha, \beta$) is the load current of the traction power supply arm, i_{cx} ($x = \alpha, \beta$) is the compensation current, i_{sx} ($x = \alpha, \beta$) is the total current of the traction power supply arm after compensation.

B. Main Circuit Topology of MM-RPC

The main circuit structure of MM-RPC is shown in Fig. 1, which is connected across two traction feeders. Taking the α-phase converter as an example, it is composed of two-phase legs connected in parallel. Each phase leg is composed of the upper and lower arms in series via the respective arm inductor L_{arm}. The midpoint of the two-phase legs is led out and connected to the traction feeder through the grid-side filter inductor L_{xf} ($x = a,b$). Each upper and lower arm is composed of *N* half-bridge SMs, i_{xy} ($x = p,n$ and $y = a,b$) is the current of each arm, and $i_{c\alpha}$ is the output ac current of the α-phase converter. The electrical parameters of the β-phase converter are the same as those of the α-phase converter, and its topology is symmetrical about the dc side. A back-to-back (BTB) structure is formed by α and β-phase converter, with the dc bus voltage in the middle, where *P* and *N* are the positive and negative ends of the high-voltage dc bus.

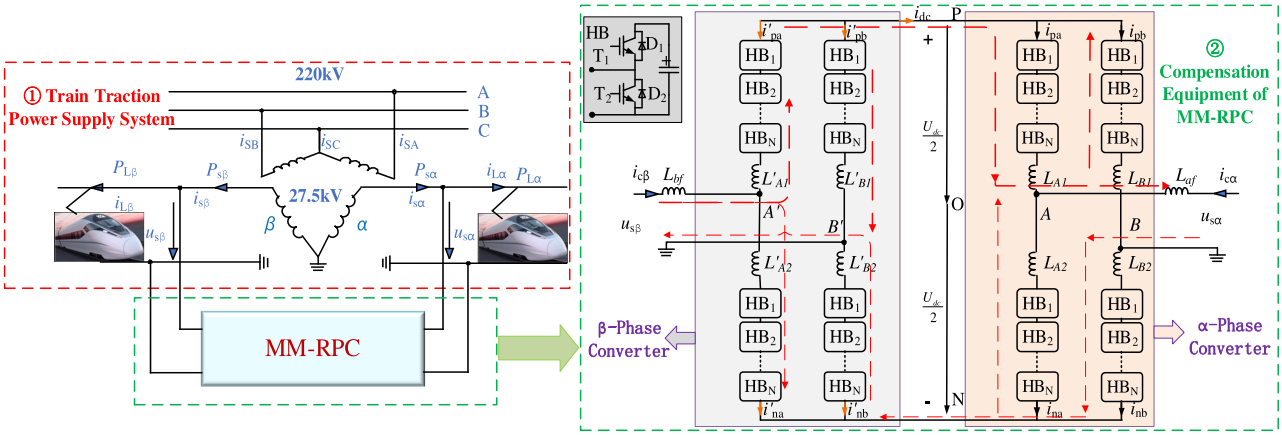

Fig. 1. V/v traction power supply system and MM-RPC compensation system.

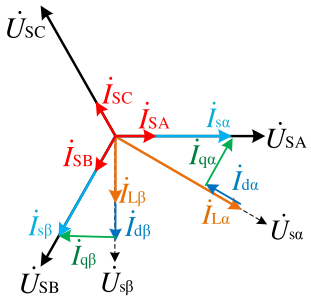

Fig. 2. MM-RPC voltage and current vector diagram.

C. Working Principle and Mathematical Model of MM-RPC

Active power should be transferred between the two traction feeders once the load is asymmetrical on both sides. Since AC drive system is adopted in most of the existing electric locomotives, the power factor of the two traction grids is close to 1. The vector diagram of the voltage and current of the transformer primary and secondary sides can be obtained as shown in Fig. 2. $\dot{I}_{da}$ and $\dot{I}_{d\beta}$ represent the load current vectors of the two traction feeders, respectively, and the load currents are not equal ordinarily, which causes the negative sequence component of the three-phase grid-side current. In order to eliminate the negative sequence components of grid current, half of the current difference between the two traction feeders is calculated [22], which is used as the active current component that needs to be transferred in the following:

$$\left|\dot{I}d\alpha\right| = \left|\dot{I}d\beta\right| = |IL\alpha - IL\beta|/2. \tag{1}$$

Moreover, the reactive power component of each converter needs to be compensated as follows:

$$\left|\dot{I}q\alpha\right| = \left|\dot{I}q\beta\right| = \tan 30^\circ \cdot |IL\alpha + IL\beta|/2. \tag{2}$$

According to the compensation regulation, the voltage and current on the three-phase grid side are kept in phase after compensation as shown in Fig. 2, and the power factor on the three-phase grid is 1. Therefore, this regulation is also named full compensation.

According to the main circuit topology of MM-RPC and Kirchhoff's law of the circuit, the a-phase leg expression is obtained as follows:

$$\begin{cases} u_{pa} + L_{\text{arm}} \cdot \frac{di_{pa}}{dt} + R_{\text{arm}} \cdot i_{pa} + u_{\text{AO}} = \frac{U_{\text{dc}}}{2} \\ u_{na} + L_{\text{arm}} \cdot \frac{di_{na}}{dt} + R_{\text{arm}} \cdot i_{na} - u_{\text{AO}} = \frac{U_{\text{dc}}}{2}. \end{cases} \tag{3}$$

The expression of the ac traction feeder is obtained

$$u_{\text{AO}} + L_{af} \cdot \frac{di_{ca}}{dt} + R_{af} \cdot i_{ca} = \frac{u_{s\alpha}}{2} \tag{4}$$

where R_{arm} and R_{af} are the arm resistor and grid-side resistor, respectively, which can be neglected due to its small value. u_{AO} is the electric potential of phase leg A.

Combined with (4), (3) can be simplified as follows:

$$\begin{cases} \frac{u_{pa}+u_{na}}{2} = \frac{U_{\text{dc}}}{2} - L_{\text{arm}} \cdot \frac{di_{\text{cira}}}{dt} \\ \frac{u_{na}-u_{pa}}{2} = \frac{u_{sa}}{2} - \left(\frac{L_{\text{arm}}}{2} + L_{af}\right) \cdot \frac{di_{ca}}{dt} \end{cases} \tag{5}$$

$$\begin{cases} i_{\text{cira}} = \frac{i_{pa}+i_{na}}{2} \\ i_{ca} = i_{na} - i_{pa} \end{cases} \tag{6}$$

where $i_{\text{cir}x}$ is the circulating current of x arm. It can be inferred that the power control on the ac side and the dc side can be achieved by controlling the arm voltages of u_{px} and u_{nx} ($x = a, b$) reasonably.

III. Reliability Analysis of MM-RPC

A. Loss Calculation of MM-RPC

The loss of SMs devices in MM-RPC can be divided into two parts: the conduction loss and the switching loss. The two parts of loss can be calculated separately as follows.

1) Conduction Loss: The upper arm of a-phase leg is taken as an example in the α-phase converter, the modulation signal of the upper arm can be written as

$$d = \frac{1}{2}\left(1 - m\sin\left(\omega t\right)\right) \tag{7}$$

where m is the voltage modulation index, which can be defined as

$$m = \frac{U_m}{U_{\rm dc}} \tag{8}$$

where U_m is the voltage amplitude of ac traction feeders, $U_{\rm dc}$ is the dc bus voltage.

The ac grid-side current $i_{c\alpha}$ can be expressed as

$$i_{ca} = I_m \sin(\omega t - \varphi) \tag{9}$$

where φ is the angle between grid voltage and current, and I_m is the amplitude of ac current.

The upper arm current i_{pa} can be derived as

$$i_{pa} = \frac{I_{\rm dc}}{2} + \frac{I_m}{2}\sin(\omega t - \varphi). \tag{10}$$

According to the power balance of ac and dc terminals, the following expression is obtained:

$$U_{\rm dc} \cdot I_{\rm dc} = \frac{U_m I_m}{2}\cos\varphi. \tag{11}$$

Based on the voltage and current equations of the upper arm, the conduction loss of the devices can be obtained as follows:

$$\begin{cases} P_{T1\_\rm con} = \frac{1}{2\pi}\int_{\pi+\varphi+\theta}^{2\pi+\varphi-\theta} -d \cdot i_{pa}(t) \cdot V_{\rm CE}(i_{pa}) d(\omega t) \\ P_{D1\_\rm con} = \frac{1}{2\pi}\int_{\varphi-\theta}^{\pi+\varphi+\theta} d \cdot i_{pa}(t) \cdot V_D(i_{pa}) d(\omega t) \\ P_{T2\_\rm con} = \frac{1}{2\pi}\int_{\varphi-\theta}^{\pi+\varphi+\theta} (1-d) \cdot i_{pa}(t) \cdot V_{\rm CE}(i_{pa}) d(\omega t) \\ P_{D2\_\rm con} = \frac{1}{2\pi}\int_{\pi+\varphi+\theta}^{2\pi+\varphi-\theta} -(1-d) \cdot i_{pa}(t) \cdot V_D(i_{pa}) d(\omega t) \end{cases} \tag{12}$$

where $\rm V_{CE}$ and $\rm V_D$ are the conduction voltage drop of IGBT and diode respectively, and θ is the angle passing through zero point of arm current. The relationship between θ and the power factor angle can be written as

$$\theta = \arcsin\left(\frac{m\cos\varphi}{2}\right). \tag{13}$$

2) Switching Loss: There are turn-ON energy and turn-OFF energy during the transient process of switching. The energy is related to the voltage and transient current across the device, which can be obtained from the datasheet. Therefore, the average switching loss of the device in a fundamental period can be derived as

$$\begin{cases} P_{T\_\rm sw} = \sum_{i=1}^{n}\left[E_{{\rm on}i}(i_T, V_{\rm CE}) + E_{{\rm off}i}(i_T, V_{\rm CE})\right] \\ P_{D\_\rm sw} = \sum_{i=1}^{n}\left[E_{{\rm rec}i}(i_D, V_D)\right] \end{cases} \tag{14}$$

where $E_{{\rm on}i}$ is the turn-ON energy, $E_{{\rm off}i}$ is the turn-OFF energy, $E_{{\rm rec}i}$ is the reverse recovery energy of diode, and n is the number of switching times during a fundamental period.

The total loss in a fundamental period by the above analysis can be obtained as follows:

$$\begin{cases} P_T = P_{T\_\rm con} + P_{T\_\rm sw} \\ P_D = P_{D\_\rm con} + P_{D\_\rm sw}. \end{cases} \tag{15}$$

Under NLM, the switching loss and the conduction loss of the device under the unbalanced traction load are significantly different. To facilitate analysis, the relationship curve between conduction loss and power factor angle can be drawn in Fig. 3. As the low switching frequency, the conduction loss of the semiconductor is dominant compared with the switching loss

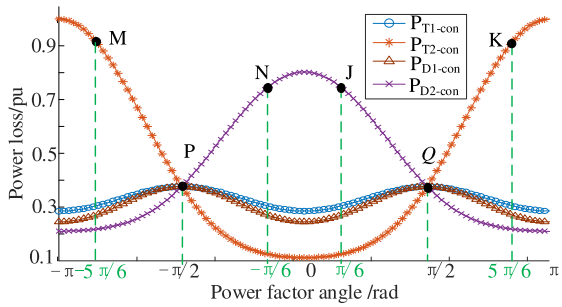

Fig. 3. Relationship between the conduction loss and power factor angle of SMs devices.

[23]. Therefore, conduction loss is adjusted to improve device reliability in this article. In full compensation mode, the distribution characteristics of conduction loss can be obtained as follows.

1) When $P_{L\alpha} = P_{LN}$, $P_{L\beta} = 0$, the maximum loss corresponds to point $M(P_{T2\text{-con}})$ at $\varphi_\alpha = -5\pi/6$ (α-phase converter), and the maximum loss corresponds to point $J(P_{D2\text{-con}})$ at $\varphi_\beta = \pi/6$ (β-phase converter).
2) When $P_{L\alpha} = 0$, $P_{L\beta} = P_{LN}$, the maximum loss corresponds to point $N(P_{D2\text{-con}})$ at $\varphi_\alpha = -\pi/6$ (α-phase converter), and the maximum loss corresponds to point $K(P_{T2\text{-con}})$ at $\varphi_\beta = 5\pi/6$ (β-phase converter).
3) When $P_{L\alpha} = P_{L\beta}$, the loss of the two converter devices are located at points P and Q. At this time, the loss consistency of the two converters is the best.
4) When $P_{L\alpha} \neq P_{L\beta}$, the φ_α of α-phase converter belongs to $(-5\pi/6, -\pi/6)$, and the φ_β of β-phase converter belongs to $(\pi/6, 5\pi/6)$.

It can be found that the conduction loss and fluctuation of $T2$ and $D2$ are the largest. Thus, the conduction loss of $T2$ and $D2$ are preliminarily selected as the objective functions to be optimized.

B Junction Temperature Calculation

In order to obtain the junction temperature of the device more accurately, it is not only necessary to know the loss of the device, but also to obtain the thermal network. The typical packaging process of the device is exhibited in Fig. 4(a). The equivalent thermal resistance network model of the packaging process is obtained in Fig. 4(b). Furthermore, the fourth-order foster model from the chip to the baseplate, which can be derived from the device datasheet. The green diagram is the first-order thermal resistance model of thermal grease, and the blue diagram is the first-order thermal resistance between the heat sink and the ambience.

Combined with all those loss, the calculation expression of junction temperature can be further obtained

$$\begin{cases} T_{j\_T} = P_T(Z_{T\_\rm th\_JC} + Z_{T\_\rm th\_CH}) \\ \qquad + (P_T + P_D)Z_{\rm th\_HA} + T_a \\ T_{j\_D} = P_D(Z_{D\_\rm th\_JC} + Z_{D\_\rm th\_CH}) + (P_T \\ \qquad + P_D)Z_{\rm th\_HA} + T_a \end{cases} \tag{16}$$

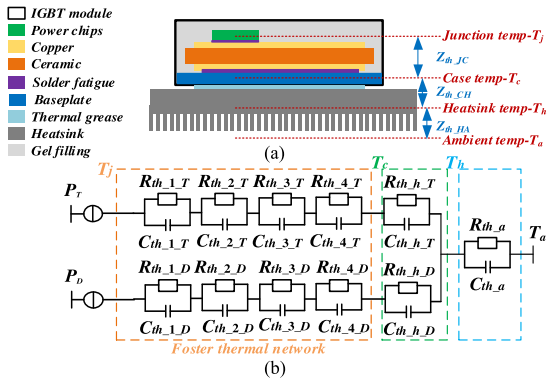

Fig. 4. Structure of device package and thermal resistance model diagram. (a) Packaging structure of the device. (b) Diagram of equivalent thermal resistance model.

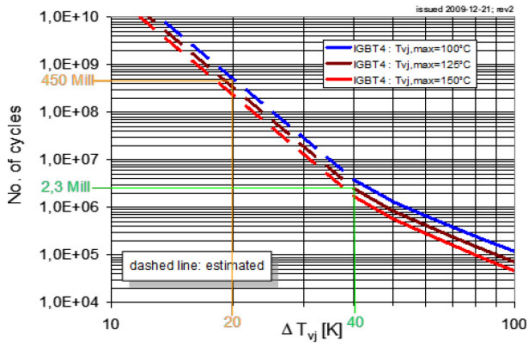

Fig. 5. Curve of power cycle capability [11].

where T_{j_T} and T_{j_D} are the junction temperature of IGBT and diode. $Z_{T\_th\_JC}$ is the thermal resistance between chip and case. $Z_{T\_th\_CH}$ is the thermal resistance between case and heatsink. Z_{th_HA} is the thermal resistance between heatsink and ambient air. T_a is the ambient temperature.

C. Lifetime Calculation of MM-RPC

In order to analyze the device lifetime effect of thermal stress caused by device junction temperature, the types of thermal load that semiconductor devices bear and the number of cycles of each thermal load are counted by the rain flow counting method. Then, the total number of power cycles that the semiconductor device withstands under each thermal load can be calculated. Finally, according to Miner's linear cumulative damage theory, the lifetime expectancy of the semiconductor device is estimated.

The number of power cycles of the semiconductor module is shown in Fig. 5. It can be found that the number of power cycles is not only affected by the average junction temperature T_{vj}, but also by the junction temperature swing ΔT_{vj}. The lower the average junction temperature, the smaller the junction temperature swing, and the more the number of power cycles. In this article, the most commonly used Coffin–Manson–Arrhenius life model [24] is selected as the lifetime model of devices. The lifetime model is shown in the following:

$$N_f = A(\Delta T_j)^{-\alpha} e^{\frac{E_a}{k_B(T_m+273)}} \tag{17}$$

where N_f is the number of cycles before failure, ΔT_j is the junction temperature fluctuation value of the device, T_m is the average junction temperature of the device, k_B is the Boltzmann constant, E_a is the excitation of the silicon chip energy. A and α are fitting coefficients, which can be obtained through accelerated aging experiments.

The damage accumulation theory is usually adopted to determine the lifetime of semiconductor devices under different time scales and thermal stress conditions. In the cumulative damage theory, the Miner method regards the damage as uniform, and the calculation is simple and convenient for application. Therefore, Miner's linear cumulative damage theory [25] is widely used in the calculation of the lifetime of semiconductor devices, as shown in the following:

$$D = \sum \frac{N_i}{N_{fi}} \tag{18}$$

where D is the cumulative damage degree. N_i is the cumulative number of cycles, and N_{fi} is the number of cycles that cause the semiconductor device to fail under the ith thermal cycle. When $D = 1$, it is judged that the semiconductor device has failed.

IV. Proposed MM-RPC Reliability Improvement Control Strategy

According to the statistical analysis of SM device loss and the junction temperature in [26], it can be concluded that the junction temperature and temperature swings of $D2$ in the rectification state are higher than that of $T2$ in the inversion state. Moreover, it can be seen from Fig. 5 that the lifetime of the device is affected by the junction temperature fluctuation ΔT_j and the average junction temperature T_j. Therefore, the lifetime of MM-RPC devices can be improved from the following two aspects.

1) Reduce the average junction temperature T_j.
2) Reduce the junction temperature fluctuation ΔT_j.

For MM-RPC, the α-phase converter and β-phase converter can be mutually converted into rectifier and inverter. When the power of the two traction feeders is seriously asymmetrical, the junction temperature swing of $D2$ (whether α or β) is the largest, which results in the reduction of the number of power cycles. Therefore, the $D2$ conduction loss is selected as the objective function to be optimized.

A. Loss Optimization Based on Incomplete Compensation

The full compensation method is ideal in the traction system. Although this method can achieve good power quality compensation, its thermal control freedom is limited. Therefore, it is difficult to adjust the thermal performance of the equipment under full compensation. Considering that the actual three-phase power system has a certain tolerance range for the power quality requirements, a PHIC control from the perspective of reliability is proposed in this article.

The proposed PHIC control not only satisfies the power quality standards of the three-phase power grid but also improves the reliability of the converter. The severe asymmetric load of two traction feeders is taken as an example for analysis. I_{dx} and $I_{qx}(x = \alpha, \beta)$ represent the references of active and reactive

current, respectively. Based on the minimum conduction loss of the D2, the objective function can be obtained as follows.

1) Objective Function:

$$f(I_{d\alpha}, I_{d\beta}, I_{q\alpha}, I_{q\beta}) = \min\left(\max(P_{D2\alpha}, P_{D2\beta})\right) \tag{19}$$

$$P_{D2\mathrm{x}} = \frac{V_{\mathrm{CEon}}}{4T} I_{m\mathrm{x}} \times \left[\left(2 + m^2 \cos^2\varphi_{\mathrm{x}}\right)\cos\theta_{\mathrm{x}} - \left(\pi - 2\theta_{\mathrm{x}} + \sin 2\theta_{\mathrm{x}}\right)\frac{m\cos\varphi_{\mathrm{x}}}{2}\right] \tag{20}$$

where V_{CEon} is the equivalent conduction voltage drop, and T is the period of grid.

Combined with the relationship of I_{mx}, φ_{x} and I_{dx}, I_{qx}

$$I_{m\mathrm{x}} = \sqrt{{I_{d\mathrm{x}}}^2 + {I_{q\mathrm{x}}}^2} \tag{21}$$

$$\varphi_{\mathrm{x}} = \arctan\left(\frac{I_{q\mathrm{x}}}{I_{d\mathrm{x}}}\right) \tag{22}$$

$$\theta_{\mathrm{x}} = \arcsin\left(\frac{m\cos\varphi_{\mathrm{x}}}{2}\right) \tag{23}$$

where $x = \alpha, \beta$.

2) Constraints:

a) Constraint of three-phase voltage unbalance: Three-phase currents can be obtained after compensation

$$\begin{cases} \dot{I}_{\mathrm{SA}} = \left(\dot{I}_{L\alpha} - \dot{I}_{d\alpha}\right)\cdot e^{-j\frac{\pi}{6}} + \dot{I}_{q\alpha} e^{j\frac{\pi}{3}} \\ \dot{I}_{\mathrm{SB}} = \left(\dot{I}_{L\beta} + \dot{I}_{d\beta}\right)\cdot e^{-j\frac{\pi}{2}} + \dot{I}_{q\beta} e^{j\pi} \\ \dot{I}_{\mathrm{SC}} = -\left(\dot{I}_{\mathrm{SA}} + \dot{I}_{\mathrm{SB}}\right). \end{cases} \tag{24}$$

The negative sequence current can be written as

$$\left|\dot{I}_{-}\right| = \left|\dot{I}_{\mathrm{SA}} + \dot{I}_{\mathrm{SB}}\cdot e^{-j\frac{2\pi}{3}} + \dot{I}_{\mathrm{SC}}\cdot e^{j\frac{2\pi}{3}}\right|. \tag{25}$$

Since the active power transferred by the converters on both sides of the MM-RPC is the same, the following formula can be obtained as

$$I_{d\alpha} = -I_{d\beta} = I_d. \tag{26}$$

Then, three-phase voltage unbalance factor can be obtained as

$$\varepsilon_u = \frac{\sqrt{3}\cdot I_{-}\cdot U}{S_K} * 100\% \le 1.2\% \tag{27}$$

where U is the line voltage rms of three-phase grid-side, and S_K represents the short-circuit capacity of the transformer.

b) Grid-side power factor: In order to ensure the power factor of the three-phase system and reduce the loss of the system, the active power and reactive power compensated by the converter should satisfy the following:

$$P_{L\alpha} + P_{L\beta} \ge \cos\varphi^* \cdot \sqrt{\left(P_{L\alpha} + P_{L\beta}\right)^2 + \left(Q_\alpha + Q_\beta\right)^2} \tag{28}$$

where Q_α and Q_β are the values that need to be compensated by the two converters, respectively. $\cos\varphi^*$ is the power factor standard of the three-phase system.

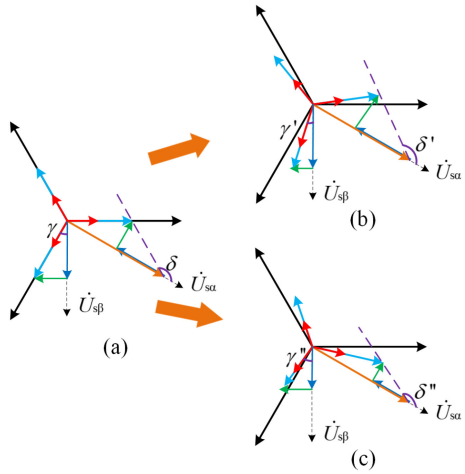

Fig. 6. Vector diagrams of different compensation methods.

c) Capacity constraints of converters on both sides: The capacity of the converters on both sides can be derived as follows:

$$\begin{cases} \frac{1}{2}U_{sa}\cdot\sqrt{{I_{d\alpha}}^2 + {I_{q\alpha}}^2} \le S_\alpha \\ \frac{1}{2}U_{s\beta}\cdot\sqrt{{I_{d\beta}}^2 + {I_{q\beta}}^2} \le S_\beta \end{cases} \tag{29}$$

where S_α and S_β are the capacity of the two converters.

d) Active power constraint: The loss deviation of the SMs devices can be reflected by the active power transferred by MM-RPC. In order to illustrate the two cases of transferring active power, the voltage and current vector diagrams are drawn in Fig. 6.

Two compensation modes are compared, although the negative sequence unbalance and power factor of the three-phase grid-side can meet the requirements under the two compensation methods, the active current transferred by mode I is greater than that in mode II. Thus, the loss of SMs devices is further aggravated in mode I, which can be found in Section II. In order to avoid operating in the incomplete compensation mode I, another constraint condition is added for the transferred active power

$$\left|I_{d\alpha,\beta}\right| < \left|I_{L\alpha} - I_{L\beta}\right|/2. \tag{30}$$

e) Constraints of grid-connected current: In order to ensure that the loss in incomplete compensation is better than the full compensation, the grid-connected current amplitude constraints have been added as follows:

$$\begin{cases} {I_{d\alpha}}^2 + {I_{q\alpha}}^2 \le \frac{1}{3}\left(\frac{\left(I_{L\alpha}+I_{L\beta}\right)^2}{4}\right) + \frac{\left(I_{L\alpha}-I_{L\beta}\right)^2}{4} \\ {I_{d\beta}}^2 + {I_{q\beta}}^2 \le \frac{1}{3}\left(\frac{\left(I_{L\alpha}+I_{L\beta}\right)^2}{4}\right) + \frac{\left(I_{L\alpha}-I_{L\beta}\right)^2}{4}. \end{cases} \tag{31}$$

Therefore, the reference current value that satisfies the condition of junction temperature optimization can be obtained from objective function and constraints.

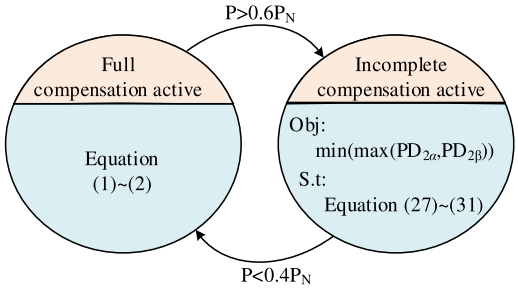

Fig. 7. Power hysteresis compensation strategy.

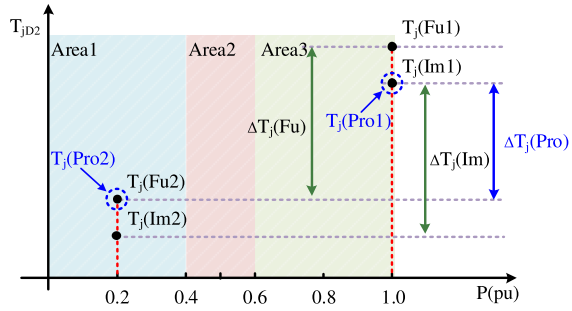

Fig. 8. Schematic diagram of power hysteresis strategy to reduce junction temperature fluctuations.

B. Junction Temperature Fluctuation Reduction Based on Power Hysteresis

Because the loads of the traction feeders are severely asymmetric, an incomplete compensation is adopted. On the one hand, the converter capacity can be reduced, and on the other hand, the average junction temperature effect can be improved. When the difference of loads between the two traction feeders is small, the junction temperature fluctuation can be decreased, which is particularly important for improving the reliability of the device. The active power to be transferred by converters on both traction feeders can be obtained as

$$P_{\text{trans}}=\frac{U\cdot|I_{L\alpha}-I_{L\beta}|}{2}. \tag{32}$$

Under the full load asymmetrical conditions, define the power to be transferred as the rated value P_N is $P_{N\text{trans}}$, the following formula can be obtained as:

$$P_{N\text{trans}}=\frac{U\cdot|I_{L\alpha N}-0|}{2}=\frac{U\cdot|0-I_{L\beta N}|}{2}. \tag{33}$$

A schematic diagram of PHIC control is shown in Fig. 7. The full compensation and incomplete compensation are determined by the power threshold, and the intermediate value $0.5P_{N\text{trans}}$ is selected as the critical threshold. When the converter power is close to the threshold, the operating mode of the converter is inevitably switched frequently due to power fluctuations, which impacts the stable operation of the system. Therefore, a hysteresis width of $0.1P_{N\text{trans}}$ is set to avoid this phenomenon. When the transferred power $P<0.4P_N$, the full compensation mode based on (1) and (2) is activated. When $P>0.6P_N$, the incomplete compensation mode of the converter is activated, and the current references required of MM-RPC are determined by the objective function and the constraint equations (27)–(31).

In order to characterize the ability of the proposed PHIC strategy to improve junction temperature fluctuations, the principle of the proposed strategy is illustrated in Fig. 8. According to the power variation range of the converter, it is divided into three areas: Area1, Area2, and Area3. Among them, Area1 $\in$ [0, $0.4P_N$], Area2 $\in$ ($0.4P_N$, $0.6P_N$], and Area3 $\in$ ($0.6P_N$, $1.0P_N$]. The junction temperature under full compensation and incomplete compensation is T_j(Fu) and T_j(Im). The junction temperature under the proposed compensation control is Tj(Pro). Assuming that at the moment k $-$ 1, the converter operating point is located in Area3 (such as $1.0P_N$), and the junction temperatures corresponding to the three different control strategies are T_j(Fu1), T_j(Im1), and T_j(Pro1). At the moment k, the converter point is transferred in Area1 (such as $0.2P_N$). The corresponding junction temperatures of the three different control strategies are T_j(Fu2), T_j(Im2), and T_j(Pro2). The junction temperature fluctuations ΔT_j(Fu), ΔT_j(Im), and ΔT_j(Pro) corresponding to the three operating conditions are calculated, respectively, and the following relationships can be found as follows:

$$\Delta T_j\,(\text{Pro})\le\Delta T_j\,(\text{Im})\,. \tag{34}$$

C. System Control Strategy

The block diagram of the proposed PHIC control of MM-RPC is shown in Fig. 9. First, the traction feeder voltages $u_{s\alpha}$, $u_{s\beta}$ and load currents $i_{L\alpha}$, $i_{L\beta}$ are sampled, and the voltage angular frequency is obtained by the phase-locked loop (PLL). Then, the d-q component of traction feeders and load currents can be obtained. The power difference between two traction feeders is calculated by (32). Then, the power difference and the critical power point of the power hysteresis are compared, and the compensation mode is selected according to Fig. 7. If the full compensation mode is adopted, the current reference value can be obtained through (1) and (2). In addition, if the incomplete compensation method is adopted, the reference value can be calculated according to (19)–(31). Through the d-q transform, the d-q component of the output current can be obtained and compared with the active and reactive current references to obtain the errors. The errors are sent to the current controllers, and the outputs are inversely transformed to obtain the modulated signals. The α-phase converter adopts voltage and current dual-loop control, and the β-phase converter adopts single current loop control. Taking into account that additional loss could be brought by the second-order circulating current of the arm, the second-order circulating current suppression strategy based on the PR controller is adopted. In the modulation aspect, the NLM modulation strategy [27] is adopted. In order to reduce the switching loss, a SMs capacitor voltages sorting method is adopted.

V. Simulation Verification

In order to verify the effectiveness of the aforementioned PHIC control strategy, the MM-RPC thermo-electric

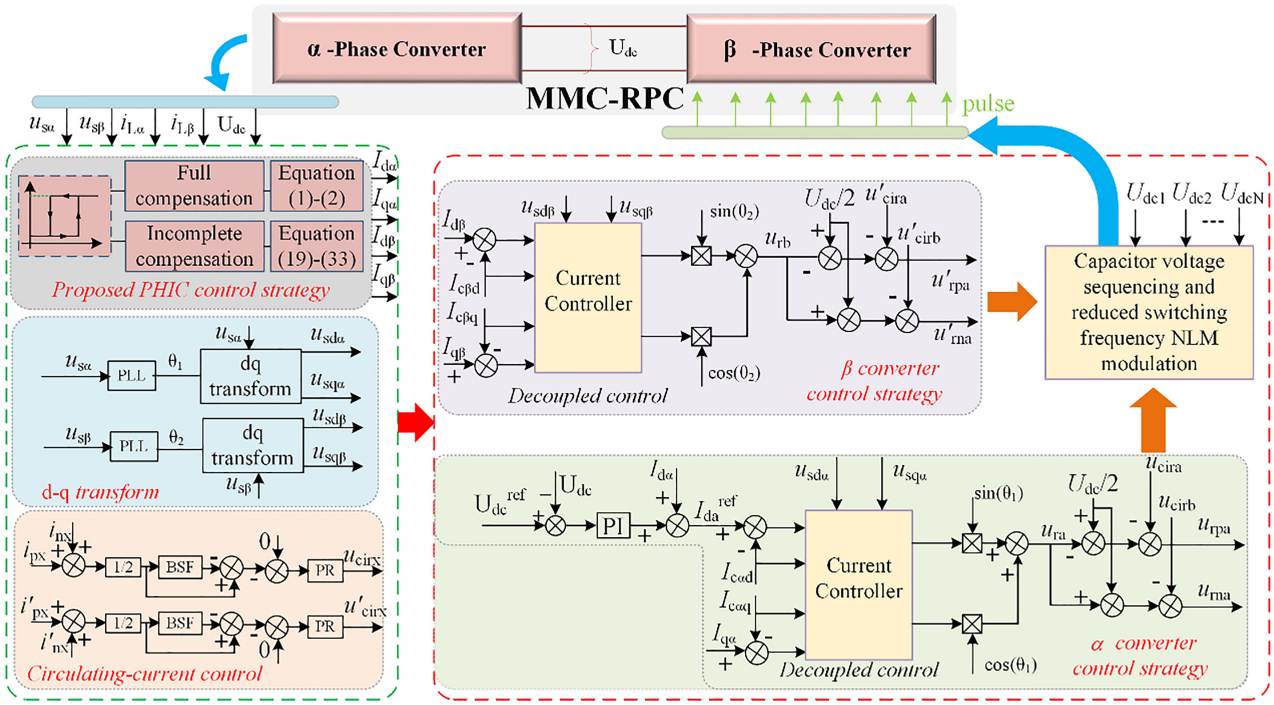

Fig. 9. System control block diagram of MM-RPC.

TABLE I
MM-RPC SYSTEM PARAMETERS

Parameters	Value
Rated capacity S	20MVA
Three-phase grid voltage U	220kV
Traction grid voltage $U_{s\alpha}$,$U_{s\beta}$	27.5kV
AC grid frequency f_s	50Hz
DC bus voltage U_{dc}	44kV
SM capacitor C_{smi}	4 mF
V/v transformer ratio k	8
SMs capacitor voltage U_{dci}	2.75kV
Maximum load of traction power $P_{L\alpha}$, $P_{L\beta}$	25.2MW
No. of SM in each leg N	32
Arm inductance L	15mH

co-simulation model shown in Fig. 1 is built on the MATLAB/PLECS simulation platform in this section. And the compensation strategies of the full compensation and PHIC control strategy are compared and analyzed in details. The IGBT power module 5SNA 0650J450300 of Hitachi ABB Power Grids is selected in the simulation model. The main electrical parameters of the simulation circuit are shown in Table I. In addition, two scenarios are considered, one is a single case study, and the other is based on the load curve of the Beijing–Shanghai high-speed rail traction substation.

A. Scenario 1: A Specified Case

In order to verify the feasibility of the above analysis and calculation, the different load conditions of the traction feeders are analyzed. The load conditions of the traction grid are expressed as follows. Between 1 and 2 s, the α-side traction feeder is fully loaded, while the β-side is no-load. At 2 s, the load of the α-side traction feeder is reduced to 60%P_N, while the β-side is increased to 20%P_N. At 3 s, the traction feeder on the α-side becomes no-load, while the β-side is 60%P_N. At 4 s, the α-side power supply arm is no-load, while the β-side is fully loaded. At 5 s, the traction feeders on both sides are no-load.

1) Full Compensation: In the full compensation mode, the three-phase grid-side current waveforms are shown in Fig. 10(a). The voltage unbalance factor of the three-phase grid is 0 during the full compensation, and the grid-side power factor is 1, in which the unity power factor operation can be achieved. The arm circulating current of the α and β-phase converters are showed in Fig. 10(b). At 1 s, the second-order circulating current suppression of the bridge arm is realized effectively by the PR circulating current controller.

2) Proposed Compensation Strategy: In the proposed PHIC, the three-phase grid-side current waveforms are shown in Fig. 11(a). The negative sequence unbalance factor of the grid-side voltage is 3.575% without compensation, and 1.2%, 0, 1.2%, and 1.2% after compensation under different loads. The power factor of the three-phase grid side is 1 without compensation, and 0.998, 1, 0.996, and 0.998 after compensation under different loads. Fig. 11(b) shows the circulating current of the bridge arms of the α and β-phase converters. Compared with the full compensation method, when the power difference of both traction loads is less than 0.4*PN*, the full compensation is realized. The current of bridge arms of the two compensation methods keeps all the same. When the load difference of both traction loads is greater than 0.6*PN*, the amplitude of the circulating current of the incomplete compensation is less than that of the full compensation.

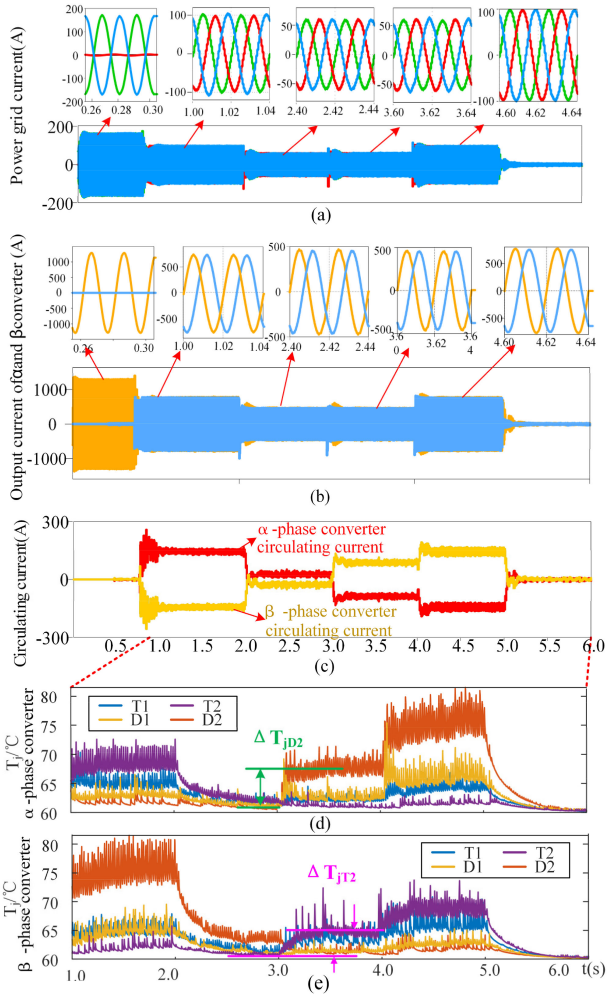

Fig. 10. Three-phase grid-side voltage, current and converter circulating current in full compensation mode. (From top to bottom: power grid current, output current of α-phase and β-phase converter, circulating current, junction temperature of α-phase converter, and junction temperature of β-phase converter.)

TABLE II
COMPARISON OF DEVICE LIFETIME BEFORE AND AFTER OPTIMIZATION

Converter	Lifetime under full compensation (years)			Lifetime under the proposed compensation (years)		
	Devices		Module	Devices		Module
α phase converter	T1	88	12	T1	7129	110
	T2	343		T2	4210	
	D1	1045		D1	1845	
	D2	12		D2	110	
β phase converter	T1	1185	18	T1	46595	203
	T2	127		T2	203	
	D1	355		D1	2712	
	D2	18		D2	259	

3) Comparison of the Junction Temperature of Two Compensation Modes: The junction temperature fluctuations of the SM devices in the full compensation and proposed PHIC control are shown in Figs. 10(c) and (d) and 11(c) and (d), respectively. The junction temperature distributions of the same converter are compared as follows. The average junction temperature of all devices has been improved in the PHIC control strategy, and the junction temperature of the device under the worst conditions

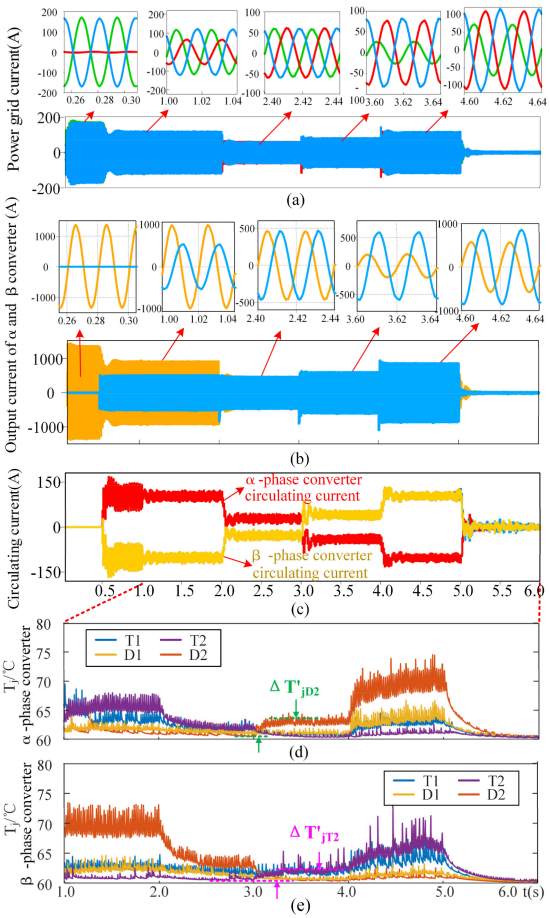

Fig. 11. Three-phase grid-side voltage, current, and converter circulating current in the proposed compensation method. (From top to bottom: power grid current, output current of α-phase and β-phase converter, circulating current, junction temperature of α-phase converter, and junction temperature of β-phase converter.)

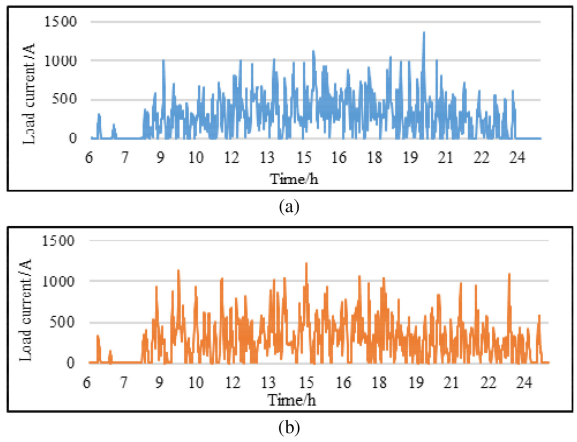

Fig. 12. Load curves of two traction feeders. (a) α-side load curve of traction substation. (b) β-side load curve of traction substation.

has improved about 5.3 °C ($D2$) and 3 °C ($T2$). In terms of junction temperature fluctuation, compared with and without the proposed control strategy, the junction temperature fluctuation of the diode $D2$ of the α-phase converter is decreased from 6 to 2 °C, and the SM $T2$ junction temperature fluctuation in

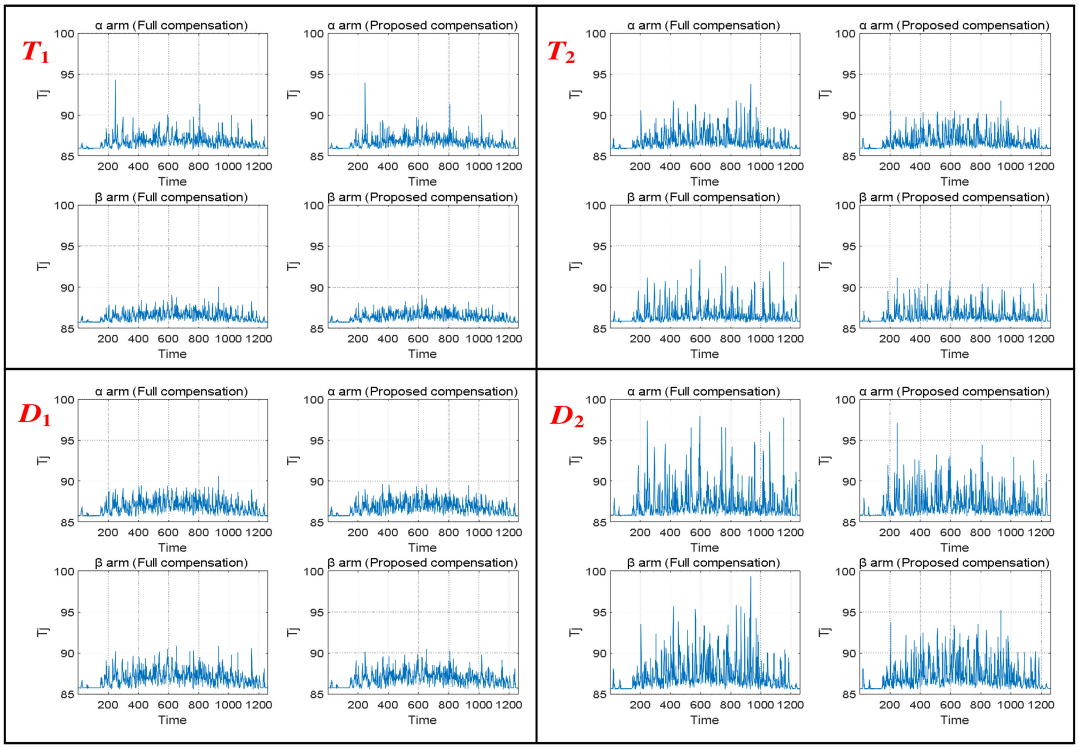

Fig. 13. Junction temperatures of the converter with and without optimization.

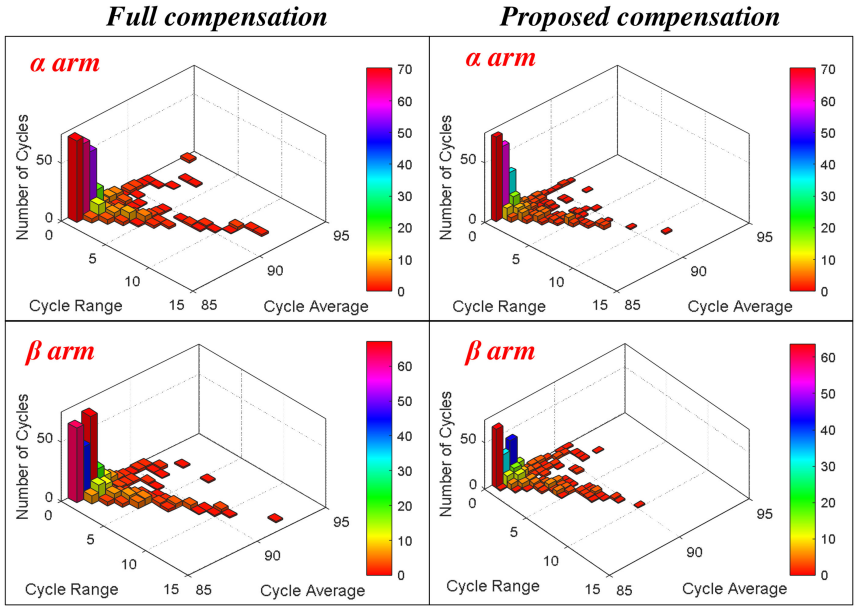

Fig. 14. Rain flow histogram with and without optimization.

the β-phase converter is decreased from 4 to 2 °C, indicating that the adoption of proposed control effectively reduces the fluctuation of junction temperature.

4) Lifetime Estimation of Two Compensation Modes: According to the lifetime calculation formula in Section III, the lifetime of each device of the SM in Figs. 10 and 11 can be estimated. The lifetime of each device in the two methods can be obtained as exhibited in Table II.

It can be noticed from Table II that the lifetime of the α-phase converter and the β-phase converter in the full compensation mode are 12 years and 18 years, respectively, while 110 years and 203 years in the proposed compensation. Therefore, the lifetime of the converters on both sides is improved, indicating that the proposed PHIC control can effectively improve the junction temperature of the device and improve the system reliability of the MM-RPC.

TABLE III
COMPARISON OF DEVICE LIFETIME BEFORE AND AFTER OPTIMIZATION

Converter	Lifetime under full compensation (years)			Lifetime under the proposed compensation (years)		
	Devices		Module	Devices		Module
α-phase converter	T1	87723	13.5816	T1	116076	48.3219
	T2	73649		T2	254069	
	D1	590813		D1	987635	
	D2	13.5816		D2	48.3219	
β-phase converter	T1	8000	18.6124	T1	20852	62.6101
	T2	202		T2	914	
	D1	965		D1	1716	
	D2	18.6124		D2	62.6101	

B. Scenario 2: A Case of Beijing–Shanghai Traction Substation

The two-phase load distribution characteristics were analyzed in [28]. In order to verify the effectiveness of the proposed control strategy applied to the actual project, the load curve of the two power supply arms of the Beijing–Shanghai high-speed railway traction substation is taken as an example. The load curves of two traction feeders are shown in Fig. 12.

1) Junction Temperature Fluctuation Based on Mission Profile: In the full compensation control and the proposed PHIC control, the junction temperatures comparison chart of each module device of α-phase converter and β-phase converter is shown in Fig. 13. It can be found that the fluctuation of the junction temperature and the average junction temperature in the proposed PHIC control are smaller than the full compensation.

2) Rain Flow Statistics: $D2$ is taken as an example to develop rain flow statistics based on its junction temperature in Fig. 14. It can be seen that in the proposed control strategy, the rain flow statistics of the α-phase converter and the β-phase converter are more concentrated in the low-temperature area. The high junction temperature swing and the high-temperature part are relatively less, and the thermal performance is significantly improved.

3) Lifetime Calculation of Devices: According to the Coffin-Manson model and the cumulative damage the lifetime of the converter is calculated, as shown in Table III. The same as the theory is that the lifetime of $D2$ in the SM is the shortest, which determines the lifetime of the entire module. By comparing the lifetime calculated under the full compensation and the proposed strategy, it can be found that the lifetime of the SM has been greatly improved. The lifetime of the α-phase converter and β-phase converter has increased from 13.6 years and 18.6 years to 48.3 years and 62.6 years, respectively. Thus, the lifetime is increased by more than three times.

VI. EXPERIMENTAL VERIFICATION

A. Construction of the Experimental Platform

In this section, the experiment is conducted to verify the correctness of the proposed strategy. An experimental platform similar to [29] is built, Infineon's half-bridge module FF150R12ME3G (1200V/150A) is used in the laboratory to build an experimental platform for the thermal-behavior evaluation of an SM in MM-RPC. The SM capacitor voltage is downscaled to 120 V for protection since the absence of the filling gel makes high voltage operation riskier. The control scheme of the platform is shown in Fig. 15(a). The drive signal of the test arm is generated by the required switching profile. Moreover, the drive signal of the load arm is generated by the PI closed-loop control of the load current. The photograph of the experimental setup is shown in Fig. 15(b). It is worth mentioning that the control scheme is realized by TI digital signal processor TMS320F28335. The ADC module is adopted to measure load current, and the ePWM module is used to generate PWM signals. The Tektronix oscilloscope MDO3024 is used to record the output waveform, and the IR camera is used to measure the junction temperature of the opened IGBT power device module.

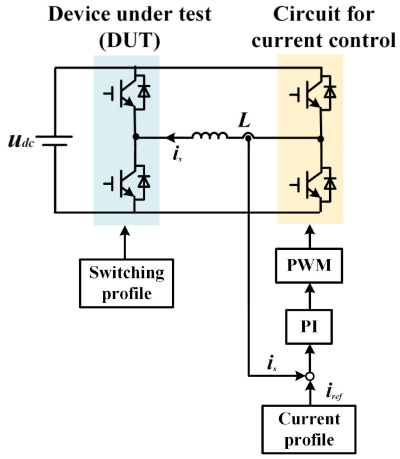

(a)

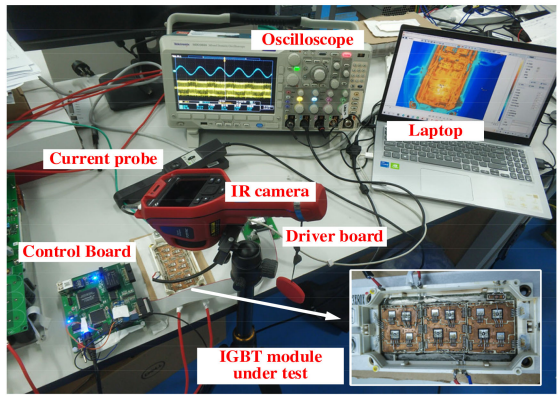

(b)

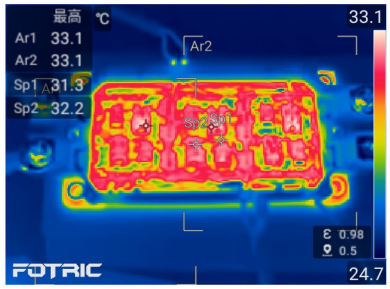

(c)

Fig. 15. Experimental platform for the thermal-behavior evaluation of an SM in MM-RPC. (a) Control block diagram. (b) Setup of the experimental bench. (c) Temperature distribution in the IGBT module recorded by IR camera.

TABLE IV
MISSION PROFILE AND COMPENSATION CURRENT VALUE

Mission Profile		Current reference	Full compensation	Proposed compensation
Case 1	$P_{L\alpha}$=10kW	I_α	5.2+13.6sin(ωt+120°)	4.26+11.2sin(ωt+120.2°)
	$P_{L\beta}$=0	I_β	-5.2+13.6sin(ωt-120°)	-4.26+10sin(ωt-117°)
Case 2	$P_{L\alpha}$=6kW	I_α	2.09+7.2sin(ωt+101°)	1.57+7.19sin(ωt+89.6°)
	$P_{L\beta}$=2kW	I_β	-2.09+7.2sin(ωt-139°)	-1.57+3.9sin(ωt-116°)
Case 3	$P_{L\alpha}$=0	I_α	-3.13+8.2sin(ωt)	-3.13+8.2sin(ωt)
	$P_{L\beta}$=6kW	I_β	3.13+8.2sin(ωt+120°)	3.13+8.2sin(ωt+120°)
Case 4	$P_{L\alpha}$=0	I_α	-5.2+13.6sin(ωt)	-4.26+10.sin(ωt-4°)
	$P_{L\beta}$=10kW	I_β	5.2+13.6sin(ωt+120°)	4.26+11.1sin(ωt+119.7°)

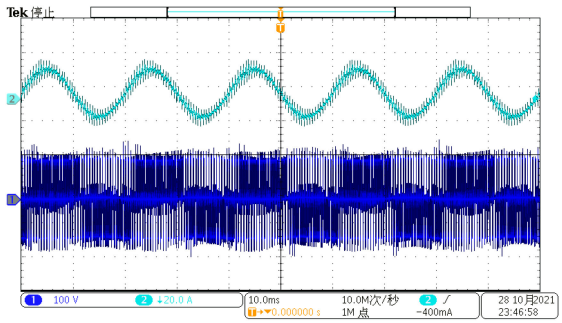

Fig. 16. Experimental waveforms of current and voltage under one profile.

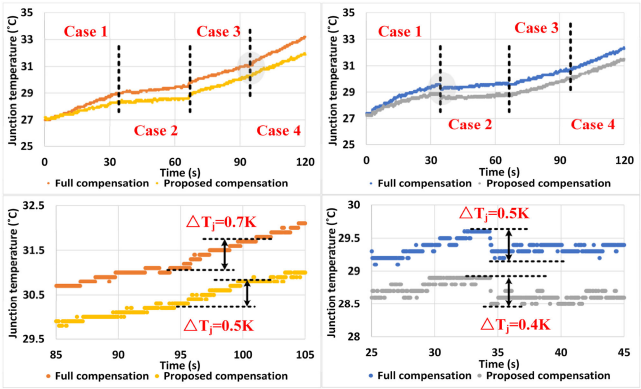

Fig. 17. Junction temperature waveform of α phase converter (left: $T2$, right: $D2$).

The temperature distribution in the IGBT module recorded by IR camera is shown in Fig. 15(c). Fig. 16 shows the experimental waveforms of current and voltage under one profile.

B. Junction Temperature Control Effect Verification

The experiment is verified under four mission profiles. The corresponding current references obtained by using the full compensation and the proposed compensation are sorted as shown in Table IV. After running for 30 s under four mission profiles, the temperature waveform of the IGBT module is observed. It is known that the temperature of $T2$ and $D2$ is the highest. Therefore, the junction temperature waveforms of $T2$ and $D2$ are organized as shown in Figs. 17 and 18. It can be seen that the rising trend of junction temperature under full compensation is obviously faster than the proposed compensation. It can be seen from the enlarged partial temperature curve that the

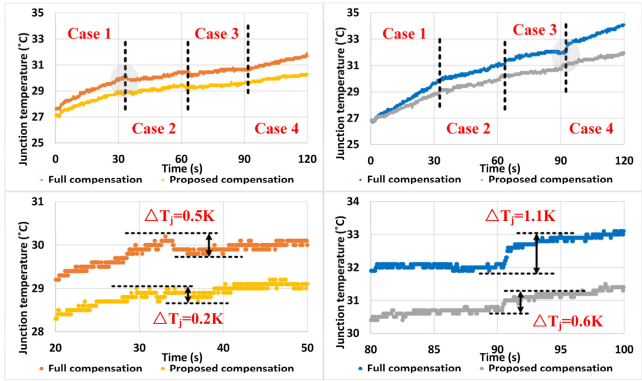

Fig. 18. Junction temperature waveform of β phase converter. (left: $T2$, right: $D2$).

junction temperature waveform under the proposed compensation is smoother and the fluctuation is smaller, which verifies the feasibility of the proposed control to improve the thermal performance of the system.

VII. CONCLUSION

In order to improve the reliability problems of MM-RPC, junction temperature optimization-based compensation strategy was proposed. First, the loss model of the power module of MM-RPC is established, and the loss distribution of power model is analyzed under different operating conditions. Then, a power hysteresis control strategy based on the incomplete compensation is proposed for MM-RPC. The full and incomplete compensation modes are reasonably selected according to the mission profiles. The proposed control strategy can effectively reduce junction temperature fluctuations under complex profiles and increase the overall lifetime of the system while meeting the power quality requirements. Finally, simulation and experimental results verify the effectiveness of the proposed control to improve the reliability of MM-RPC.

REFERENCES

[1] H. Morimoto *et al.*, "Development of railway static power conditioner used at substation for shinkansen," in *Proc. Power Convers. Conf.-Osaka 2002 (Cat. No.02TH8579)*, 2002, pp. 1108–1111.
[2] H. Wang, Y. Tian, and Q.-C. Gui, "Evaluation of negative sequence current injecting into the public grid from different traction substation in electrical railways," in *Proc. 20th Int. Conf. Exhib. Electricity Distrib.-Part 1*, 2009, pp. 1–4.
[3] S. M. Mousavi Gazafrudi, A. Tabakhpour Langerudy, E. F. Fuchs, and K. Al-Haddad, "Power quality issues in railway electrification: A comprehensive perspective," *IEEE Trans. Ind. Electron.*, vol. 62, no. 5, pp. 3081–3090, May 2015.

[4] Z. Zhang, B. Wu, J. Kang, and L. Luo, "A multi-purpose balanced transformer for railway traction applications," *IEEE Trans. Power Del.*, vol. 24, no. 2, pp. 711–718, Apr. 2009.
[5] F. F. Brenna and D. Zaninelli, "Electromagnetic model of highspeed railway lines for power quality studies," *IEEE Trans. Power Syst.*, vol. 25, no. 3, pp. 1301–1308, Aug. 2010.
[6] M. Soler, J. López, J. M. Mera Sánchez de Pedro, and J. Maroto, "Methodology for multi-objective optimization of the AC railway power supply system," *IEEE Trans. Intell. Transp. Syst.*, vol. 16, no. 5, pp. 2531–2542, Oct. 2015.
[7] H. Hu, Z. He, and S. Gao, "Passive filter design for China high-speed railway with considering harmonic resonance and characteristic harmonics," *IEEE Trans. Power Del.*, vol. 30, no. 1, pp. 505–514, Feb. 2015.
[8] R. Grunbaum, J. -P. Hasler, T. Larsson, and M. Meslay, "STATCOM to enhance power quality and security of rail traction supply," in *Proc. 8th Int. Symp. Adv. Electromech. Motion Syst. Electr. Drives Joint Symp.*, Lillie, France, 2009, pp. 1–6.
[9] L. Zhao, F. Chen, and Y. Jiang, "Research on topology and control strategy of railway power regulator based on MMC," in *Proc. 5th Int. Conf. Power Renewable Energy*, Shanghai, China, 2020, pp. 6–15.
[10] S. Yang, D. Xiang, A. Bryant, P. Mawby, L. Ran, and P. Tavner, "Condition monitoring for device reliability in power electronic converters: A review," *IEEE Trans. Power Electron.*, vol. 25, no. 11, pp. 2734–2752, May 2010.
[11] "AN2019-05_PC_and_TC_Diagrams," 2019. [Online]. Available: https://www.infineon.com/dgdl/Infineon-AN2019-05_PC_and_TC_Diagrams-ApplicationNotes-v02_01-EN.pdf?fileId=5546d46269e1c019016a594443e4396b
[12] M. Weckert and J. Roth-Stielow, "Lifetime as a control variable in power electronic systems," in *Proc. Emobility–Elect. Power Train*, Leipzig, Germany, 2010, pp. 1–6.
[13] Y. Ko, M. Andresen, G. Buticchi, and M. Liserre, "Discontinuous-modulation-based active thermal control of power electronic modules in wind farms," *IEEE Trans. Power Electron.*, vol. 34, no. 1, pp. 301–310, Jan. 2019.
[14] J. Wölfle, M. Nitzsche, J. Weimer, M. Stempfle, and J. Roth-Stielow, "Temperature control system using a hybrid discontinuous modulation technique to improve the lifetime of IGBT power modules," in *Proc. 18th Eur. Conf. Power Electron. Appl.*, Karlsruhe, Germany, 2016, pp. 1–10.
[15] J. Falck, G. Buticchi, and M. Liserre, "Thermal stress based model predictive control of electric drives," *IEEE Trans. Ind Appl.*, vol. 54, no. 2, pp. 1513–1522, Mar./Apr. 2018.
[16] M. K. Bakhshizadeh, K. Ma, P. C. Loh, and F. Blaabjerg, "Indirect thermal control for improved reliability of modular multilevel converter by utilizing circulating current," in *Proc. IEEE Appl. Power Electron. Conf. Expo.*, 2015, pp. 2167–2173.
[17] R. Han *et al.*, "Modulated model predictive control for reliability improvement of extremely low frequency power amplifier via junction temperature swing reduction," *IEEE Trans. Ind. Electron.*, vol. 69, no. 1, pp. 302–313, Jan. 2022.
[18] F. Deng, J. Zhao, C. Liu, Z. Wang, X. Cai, and F. Blaabjerg, "Temperature-balancing control for modular multilevel converters under unbalanced grid voltages," *IEEE Trans. Power Electron.*, vol. 37, no. 4, pp. 4614–4625, Apr. 2022.
[19] K. Ma, M. Liserre, and F. Blaabjerg, "Reactive power influence on the thermal cycling of multi-MW wind power inverter," *IEEE Trans. Ind Appl.*, vol. 49, no. 2, pp. 922–930, Mar./Apr. 2013.
[20] Z. Qin, M. Liserre, F. Blaabjerg, and H. Wang, "Energy storage system by means of improved thermal performance of a 3 MW grid side wind power converter," in *Proc. 39th Annu. Conf. IEEE Ind. Electron. Soc.*, Vienna, Austria, 2013, pp. 736–742.
[21] D. Zhou and F. Blaabjerg, "Optimized demagnetizing control of DFIG power converter for reduced thermal stress during symmetrical grid fault," *IEEE Trans. Power Electron.*, vol. 33, no. 12, pp. 10326–10340, Dec. 2018.
[22] C. Wu, A. Luo, J. Shen, F. J. Ma, and S. Peng, "A negative sequence compensation method based on a two-phase three-wire converter for a high-speed railway traction power supply system," *IEEE Trans. Power Electron.*, vol. 27, no. 2, pp. 706–717, Feb. 2012.
[23] S. Rohner, S. Bernet, M. Hiller, and R. Sommer, "Modulation, losses, and semiconductor requirements of modular multilevel converters," *IEEE Trans. Ind. Electron.*, vol. 57, no. 8, pp. 2633–2642, Aug. 2010.
[24] M. Andresen, K. Ma, G. Buticchi, J. Falck, F. Blaabjerg, and M. Liserre, "Junction temperature control for more reliable power electronics," *IEEE Trans. Power Electron.*, vol. 33, no. 1, pp. 765–776, Jan. 2018.
[25] M. A. Miner, "Cumulative damage in fatigue," *J. Appl. Mechanics*, vol. 12, no. 3, pp. 159–164, 1945.
[26] L. Wang, J. Xu, G. Wang, and Z. Zhang, "Lifetime estimation of IGBT modules for MMC-HVDC application," *Microelectron. Rel.*, vol. 82, pp. 90–99, Mar. 2018.
[27] X. Chen, J. Liu, S. Song, S. Ouyang, D. Wang, and Z. Deng, "Deadbeat control for circulating harmonic currents suppression of a level-increased NLM based modular multilevel converter," in *Proc. IEEE Energy Convers. Congr. Expo.*, Baltimore, MD, USA, 2019, pp. 6364–6367.
[28] S. Hu *et al.*, "A balance transformer-integrated RPFC for railway power system PQ improvement with low-design capacity," *IEEE Trans. Ind. Electron.*, vol. 65, no. 4, pp. 2925–2934, Apr. 2018.
[29] Y. Zhang, H. Wang, Z. Wang, Y. Yang, and F. Blaabjerg, "Simplified thermal modeling for IGBT modules with periodic power loss profiles in modular multilevel converters," *IEEE Trans. Ind. Electron*, vol. 66, no. 3, pp. 2323–2332, Mar. 2019.

Hongqi Ding (Student Member, IEEE) was born in Anhui, China, in 1991. He received the B.S. degree in electrical engineering and automation from Shaoyang University, Shaoyang, China, in 2015, and the M.S. degree in electrical engineering in 2018 from Hunan University, Changsha, China, where he is currently working toward the Ph.D. degree in electrical engineering with the College of Electrical and Information Engineering.

From 2018 to 2020, he was with the Department of Energy Internet Technology, CRRC ZIC Research Institute of Electrical Technology and Material Engineering, Zhuzhou, China. His research interests include modular multilevel converter, high frequency dc-dc converter, and energy router.

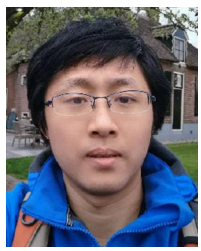

Fujun Ma (Senior Member, IEEE) was born in Hunan, China, in 1985. He received the B.S. degree in automation and the Ph.D. degree in electrical engineering from Hunan University, Changsha, China, in 2008 and 2015, respectively.

Since 2020, he has been a Professor with the College of Electrical and Information Engineering, Hunan University. His research interests include power quality managing technique of electrified railway, electric power saving, reactive power compensation, and active power filters.

Rong Han (Student Member, IEEE) was born in Gansu, China, in 1995. She received the B.S. degree in electrical engineering and automation in 2017 from Hunan University, Changsha, China, where she is currently working toward the Ph.D. degree in electrical engineering.

Her research interests include power conversion control, active thermal control, multilevel converters, and power quality control.

Lei Wang (Senior Member, IEEE) received the B.Sc. degree in electrical and electronics engineering from the University of Macau (UM), Macao, China, in 2011, the M.Sc. degree in electronics engineering from the Hong Kong University of Science and Technology (HKUST), Hong Kong, China, in 2012, and the Ph.D. degree in electrical and computer engineering from the University of Macau (UM), in 2017.

He was a Postdoctoral Fellow with the Power Electronics Laboratory, UM, from January 2017 to February 2019. He was a Visiting Fellow with the Department of Electrical and Computer Engineering, University of Auckland, Auckland, New Zealand, from February 2019 to August 2019. In 2019, he joined the College of Electrical and Information Engineering, Hunan University, Changsha, China, where he is currently a Full Professor. He has authored one Springer book, one Elsevier book chapter, five patents (U.S.A. and China), and more than 40 journal and conference papers.

Dr. Wang was the recipient of the Champion Award in the "Schneider Electric Energy Efficiency Cup," Hong Kong, in 2011, and the Macao Science and Technology R&D Award for Postgraduates (Ph.D.) in 2018.

Liheng Lin was born in Zhejiang, China, in 1997. He received the B.S degree in electrical engineering from Hunan University, Changsha, China, in 2019. He is currently working toward the Ph.D. degree with the College of Electrical and Information Engineering, Hunan University.

His research interests include electrical energy router and adaptive dynamic programming.

Qianming Xu (Member, IEEE) was born in Henan, China, in 1989. He received the B.S. degree in electrical engineering and automation and the Ph.D. degree in electrical engineering from Hunan University, Changsha, China, in 2012 and 2017, respectively.

Since 2019, he has been an Associate Professor with the College of Electrical and Information Engineering, Hunan University. His research interests include multilevel converter, power electronic reliability monitoring, and power quality control.